CrossMark

Early Results from GLASS-JWST. VIII. An Extremely Magnified Blue Supergiant Star at Redshift 2.65 in the A2744 Cluster Field

Wenlei Chen[1], Patrick L. Kelly[1], Tommaso Treu[2], Xin Wang[3,4,5], Guido Roberts-Borsani[2], Allison Keen[1], Rogier A. Windhorst[6], Rui Zhou[1], Marusa Bradac[7,8], Gabriel Brammer[9,10], Victoria Strait[9,10], Tom J. Broadhurst[11,12,13], Jose M. Diego[14], Brenda L. Frye[15], Ashish K. Meena[16], Adi Zitrin[16], Massimo Pascale[17], Marco Castellano[18], Danilo Marchesini[19], Takahiro Morishita[20], and Lilan Yang[21]

[1] School of Physics and Astronomy, University of Minnesota, 116 Church Street SE, Minneapolis, MN 55455, USA; chen6339@umn.edu
[2] Department of Physics and Astronomy, University of California, Los Angeles, 430 Portola Plaza, Los Angeles, CA 90095, USA
[3] School of Astronomy and Space Science, University of Chinese Academy of Sciences (UCAS), Beijing 100049, China
[4] National Astronomical Observatories, Chinese Academy of Sciences, Beijing 100101, China
[5] Infrared Processing and Analysis Center, Caltech, 1200 E. California Boulevard, Pasadena, CA 91125, USA
[6] School of Earth and Space Exploration, Arizona State University, Tempe, AZ 85287-1404, USA
[7] University of Ljubljana, Department of Mathematics and Physics, Jadranska ulica 19, SI-1000 Ljubljana, Slovenia
[8] Department of Physics and Astronomy, University of California Davis, 1 Shields Avenue, Davis, CA 95616, USA
[9] Cosmic Dawn Center (DAWN), Denmark
[10] Niels Bohr Institute, University of Copenhagen, Jagtvej 128, DK-2200 Copenhagen N, Denmark
[11] University of the Basque Country UPV/EHU, Department of Theoretical Physics, Bilbao, E-48080, Spain
[12] DIPC, Basque Country UPV/EHU, San Sebastian, E-48080, Spain
[13] Ikerbasque, Basque Foundation for Science, Bilbao, E-48011, Spain
[14] Instituto de Física de Cantabria (CSIC-UC), Avda Los Castros s/n. 39005 Santander, Spain
[15] Department of Astronomy/Steward Observatory, University of Arizona, 933 N. Cherry Avenue, Tucson, AZ 85721, USA
[16] Physics Department, Ben-Gurion University of the Negev, P.O. Box 653, Be'er-Sheva 84105, Israel
[17] Department of Astronomy, University of California, 501 Campbell Hall #3411, Berkeley, CA 94720, USA
[18] INAF—Osservatorio Astronomico di Roma, via di Frascati 33, I-00078 Monte Porzio Catone, Italy
[19] Department of Physics and Astronomy, Tufts University, 574 Boston Avenue, Medford, MA 02155, USA
[20] IPAC, California Institute of Technology, MC 314-6, 1200 E. California Boulevard, Pasadena, CA 91125, USA
[21] Kavli Institute for the Physics and Mathematics of the Universe, The University of Tokyo, Kashiwa, 277-8583, Japan

Abstract

We report the discovery of an extremely magnified star at redshift $z = 2.65$ in the James Webb Space Telescope (JWST) NIRISS pre-imaging of the A2744 galaxy-cluster field. The star's background host galaxy lies on a fold caustic of the foreground lens, and the cluster creates a pair of images of the region close to the lensed star. We identified the bright transient in one of the merging images at a distance of $\sim 0''.15$ from the critical curve by subtracting the JWST F115W and F150W imaging from coadditions of archival Hubble Space Telescope (HST) F105W and F125W images and F140W and F160W images, respectively. Since the time delay between the two images should be only hours, the transient must be the microlensing event of an individual star, as opposed to a luminous stellar explosion that would persist for days to months. Analysis of individual exposures suggests that the star's magnification is not changing rapidly during the observations. From photometry of the point source through the F115W, F150W, and F200W filters, we identify a strong Balmer break, and modeling allows us to constrain the star's temperature to be approximately 7000–12,000 K.

1. Introduction

Galaxies and galaxy clusters act as massive gravitational lenses that are able to magnify intrinsically faint background sources. Their magnifying power becomes greatest for intrinsically compact sources adjacent to their critical curves (or caustics in the source plane) because regions of greatest magnification are small. Indeed, the possibility that stars could become highly magnified by galaxy-cluster lenses was suggested in the early 1990s (Miralda-Escude 1991).

The first example of an extremely magnified star was a blue supergiant in a spiral galaxy at $z = 1.49$ (dubbed Icarus) discovered by Kelly et al. (2018). The star was identified in the

Hubble Space Telescope (HST) imaging of the MACS J1149.5 +2223 galaxy-cluster field taken to follow up supernova (SN) Refsdal (Kelly et al. 2015, 2016; Rodney et al. 2016; Treu et al. 2016). Microlensing of the background star by a foreground object in the lens caused its magnification to increase by a factor of approximately 3 to ~2000. The cluster lens has the effect of boosting the effective lensing effect of foreground microlenses (Venumadhav et al. 2017; Diego et al. 2018). The Spock events in an arc at $z = 1$ in the MACS J0416.1–2403 galaxy-cluster fields were probable microlensing events (Rodney et al. 2018), and a second star dubbed Warhol ($z = 0.94$, Chen et al. 2019; Kaurov et al. 2019) was identified from microlensing events found in HST imaging of the galaxy cluster. More recently, Welch et al. (2022) reported a highly magnified star dubbed Earendel at $z = 6.2$ behind the galaxy-cluster field WHL 013708. Unlike the previous examples, microlensing, which provides direct evidence that the source
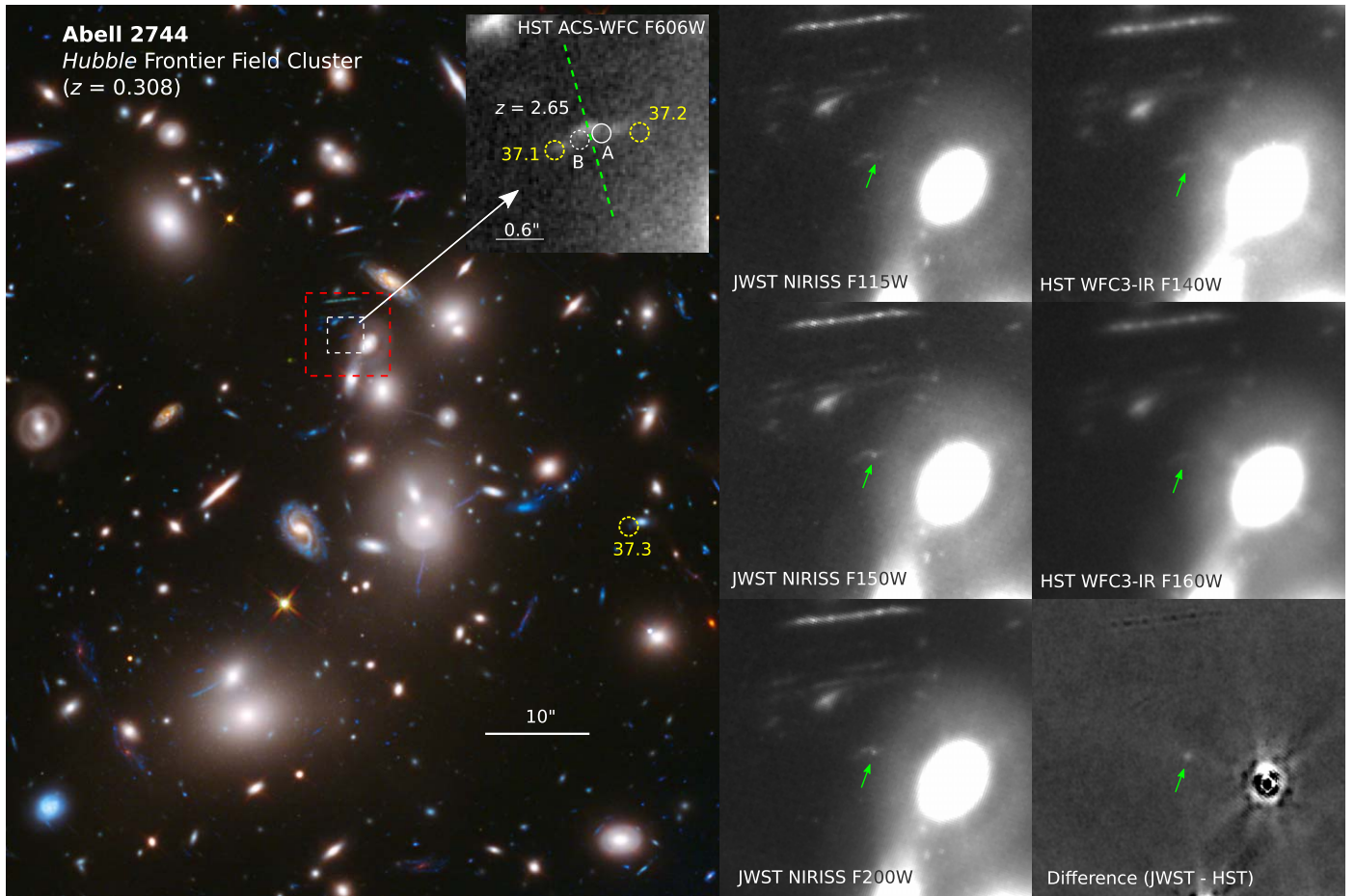
Figure 1. The left panel shows the color-composite image of the galaxy-cluster A2744 created from the HST ACS-WFC and WFC3-IR cameras and the location of the newly discovered lensed star in an arc at $z = 2.65$ (Mahler et al. 2018) in the JWST NIRISS imaging. The six panels on the right show the HST and JWST images of the region enclosed by the red dashed lines in the left panel. The three panels in the middle column show the JWST NIRISS images of the transient (green arrows) acquired by the JWST-ERS-1324 program. The top-right and the middle-right panels are coadded HST WFC3-IR F140W and WFC3-IR F160W images of the region, respectively. The bottom-right panel shows the difference image between the convolved JWST NIRISS F150W image and the combined HST template generated from WFC3-IR F140W and WFC3-IR F160W images. The inset in the top-right corner of the left panel shows the HST ACS-WFC F606W imaging of the sky region enclosed by the white dashed lines. Circle A marks the position of the newly detected transient. The green dashed line illustrates the critical curve whose location is inferred from the mirrored images of the arc. Circle B marks the position of the expected counterimage of A, and we detect no transient at that location. Yellow circles labeled 37.1, 37.2, and 37.3 are a set of multiple images listed in Table A1 in Mahler et al. (2018).

has a size of less than tens of astronomical units, has not yet been detected for Earendel, and the constraints on its size come from the galaxy-cluster lens model.

With a photon collection area a factor of 6 greater than that of HST and sensitivity across the infrared, the James Webb Space Telescope (JWST) improves our ability to detect transient events within highly magnified regions of galaxy-cluster fields. Through observations of such extreme-magnification events, we can probe individual stars at cosmological distances, including potentially individual Population III stars (Windhorst et al. 2018).

Here we report the discovery of an extremely magnified star at $z = 2.65$ in the first set of JWST images of the A2744 galaxy-cluster field, which were acquired by the GLASS-JWST program (PI: Treu; ERS-1324; Treu et al. 2022). As shown in Figure 1, the event was detected in JWST NIRISS (the Near Infrared Imager and Slitless Spectrograph; Doyon et al. 2012) imaging at a separation of $\sim 0\rlap{.}''15$ from the inferred location of the critical curve. In this paper, we describe the JWST NIRISS pre-imaging in Section 2. Section 3 provides the details of our data analysis and results. Our conclusions and discussions are

presented in Section 4. We assume a concordance Λ cold dark matter cosmological model with $\Omega_m = 0.3$, $\Omega_\Lambda = 0.7$, and a Hubble constant $H_0 = 70 \, \mathrm{km \, s^{-1} \, Mpc^{-1}}$. All magnitudes are in the AB system (Oke & Gunn 1983).

2. Data

The JWST Directors Discretionary Early Release Science Program ERS-1324 (PI T. Treu; Through the Looking GLASS: A JWST Exploration of Galaxy Formation and Evolution from Cosmic Dawn to Present Day) acquired the NIRISS imaging of the A2744 galaxy-cluster field, as the pre-imaging component to slitless spectroscopy (Roberts-Borsani et al. 2022, Paper I). A total of 24 NIRISS imaging exposures were acquired from 2022–06–28 22:04:38.674 UTC to 2022–06–29 10:41:13.507 UTC in the F115W, F150W, and F200W filters. Details on observing strategy can be found in Treu et al. (2022). We retrieved stage two images and combined the imaging using the JWST pipeline.[22]

---

[22] https://jwst-pipeline.readthedocs.io/en/latest/jwst/introduction.html

3. Data Analysis and Results

3.1. A Transient

As shown in Figure 1, the transient we report here was detected in the JWST NIRISS F150W and F200W imaging. The transient's flux did not vary significantly among the 16 F150W and F200W exposures acquired during the ~0.35 day visit to the field. There is no statistically significant detection of this transient in F115W imaging. The transient's coordinates are $\alpha = 0^h14^m21\overset{s}{.}326$, $\delta = -30°23'41\overset{s}{.}46$ in the World Coordinate System (WCS) of the official images produced by the Hubble Frontier Field survey collaboration (Lotz et al. 2017).

The transient was identified in the difference image between a convolved JWST image and the HST template. To compare HST images with the JWST NIRISS F150W image, we combined the HST WFC3-IR F140W and WFC3-IR F160W coadded images to create a template, since the wavelength range of the JWST NIRISS F150W filter is spanned by the two HST WFC3-IR filters. The effective wavelengths of the JWST NIRISS F150W, HST WFC3-IR F140W, and HST WFC3-IR F150W filters are 14846 Å, 13734 Å, and 15278 Å, respectively. We then compute a transition kernel T, for which $\mathrm{PSF_{JWST}} * T \approx \mathrm{PSF_{HST}}$, where $\mathrm{PSF_{HST}}$ and $\mathrm{PSF_{JWST}}$ are point-spread functions of the two telescopes. The kernel is determined using the Richardson–Lucy algorithm (Richardson 1972; Lucy 1974) based on a set of manually selected bright (but not saturated), isolated sources present in the imaging from both telescopes. Details are described in Appendix A. The transient is visibly apparent (with ~8σ significance) in the resulting difference image, as shown in the bottom-right panel in Figure 1.

After correcting for Galactic dust extinction ($A_V = 0.0354$ mag; Schlafly & Finkbeiner 2011), we obtain flux densities within a $0\overset{''}{.}12$ aperture centered on the transient position of 8.98 ± 7.58 nJy, 55.09 ± 7.13 nJy, and 57.28 ± 7.66 nJy for the NIRISS F115W, F150W, and F200W filters, respectively.

3.2. Underlying Arc

The redshift of the underlying arc was measured to be 2.6501 from spectroscopy acquired using the Low Resolution Imaging Spectrometer (LRIS) mounted on the Keck I telescope (Mahler et al. 2018). A so-called fold caustic creates a mirror, merging images of a galaxy that intersects it. Such a pair of mirrored images allows us to estimate the position of the critical curve. For the arc where this event has been detected, we are able to identify the critical curve's location based on the arc's morphology, as shown by the green dashed line in the inserted panel in Figure 1, where A and B label the positions of the transient and its mirrored image on opposite sides of the critical curve, respectively. In the JWST observation, no counterimage of the transient is detected.

We measure the photometry of the arc based on the official coadded images taken from the Hubble Frontier Field survey (Lotz et al. 2017). We find the total stellar mass and the star formation rate of the arc are $7.4 \times 10^7 M_\odot$ and $4.5 M_\odot \cdot \mathrm{yr}^{-1}$, respectively, without correction for lensing magnification. The surface stellar-mass density of the cluster at the position of the arc is $1.1 \times 10^7 M_\odot \cdot \mathrm{kpc}^{-2}$.

Table 1
Gravitational-lensing Properties from Published Lens Models: Magnification (μ), the 68% Confidence Interval (CI) of Magnification, Convergence (κ), and Shear (γ) at the Location of the Transient; Magnification at $0\overset{''}{.}15$ from the Local Critical Curve (μ'); and Relative Time Delay (dt) between a Pair of Counter Images at $0\overset{''}{.}15$ from the Local Critical Curve[a]

Model	μ	68% CI of μ	κ	γ	μ'	dt (hr)
		Before MUSE Spectroscopy				
Bradač (v2)[b]	55	(35, 188)	0.76	0.28	172	N/A
Zitrin-ltm-Gauss (v3)[c]	47	(36, 204)	0.73	0.34	195	1.68
Zitrin-nfw (v3)[d]	19	(14, 26)	0.85	0.24	270	3.14
		After MUSE Spectroscopy				
CATS (v4)[e]	64	(50, 89)	0.79	0.26	110	N/A
Diego (v4)[f]	84	(75, 93)	0.89	0.16	710	N/A
GLAFIC (v4)[g]	22	(20, 24)	0.80	0.28	184	0.59
Keeton (v4)[h]	31	(23, 47)	0.80	0.27	178	0.56
Sharon (v4 Cor.)[i]	282	(172, 730)	0.73	0.29	161	2.95
Williams/GRALE (v4)[j]	26	(18, 86)	0.83	0.26	160	N/A
Bergamini et al. (2022)[k]	122	(70, 423)	N/A	N/A	N/A	N/A

Notes.
[a] μ is the median value, while κ, γ, μ', and dt are based on the best-fit models available from https://archive.stsci.edu/pub/hlsp/frontier/abell2744/models/. We only evaluate the relative time delay of the Frontier Field Lens Models (Lotz et al. 2017) with resolution smaller than $0\overset{''}{.}1$ pixel^{-1}. The horizontal line separates models before and after the Multi Unit Spectroscopic Explorer (MUSE) observations of A2744 (Mahler et al. 2018).
[b] Wang et al. (2015), Hoag et al. (2016), Bradač et al. (2009, 2005).
[c] Zitrin et al. (2013, 2009) (see also Merten et al. 2009, 2011).
[d] Zitrin et al. (2013, 2009) (see also Merten et al. 2009, 2011).
[e] Mahler et al. (2018).
[f] Diego et al. (2005a, 2005b, 2007, 2015).
[g] Kawamata et al. (2018, 2016), Oguri (2010).
[h] McCully et al. (2014), Ammons et al. (2014), Keeton (2010).
[i] Johnson et al. (2014), Jullo et al. (2007).
[j] Sebesta et al. (2016), Liesenborgs et al. (2006).
[k] Bergamini et al. (2022).

3.3. Gravitational Lens Models

Using the published Frontier Fields Lens Models[23] (Lotz et al. 2017) listed in Table 1 and a recent model (Bergamini et al. 2022) for the A2744 galaxy cluster, we calculate their magnification maps at $z = 2.65$ and compare these maps with the position of the transient, as shown in Figure 2. The predicted magnification μ at the position of the newly discovered transient is listed in Table 1. For the newly released model from Bergamini et al. (2022), we obtained the magnification of the best-fit model generated from the paper's Strong Lensing Online Tool. We can see that the position of the event is close to the predicted galaxy-cluster critical curves from these lens models. The model predictions are also, in general, consistent with the multiple images of the arc, although these models' predictions for the position of the critical curve have large uncertainties. We also note that the Frontier Fields Lens Models were constructed before the spectroscopic redshift of this system was known.

The position of the transient, marked by A in the inserted image in the left panel of Figure 1, is ~$0\overset{''}{.}15$ from the inferred

---

[23] https://archive.stsci.edu/pub/hlsp/frontier
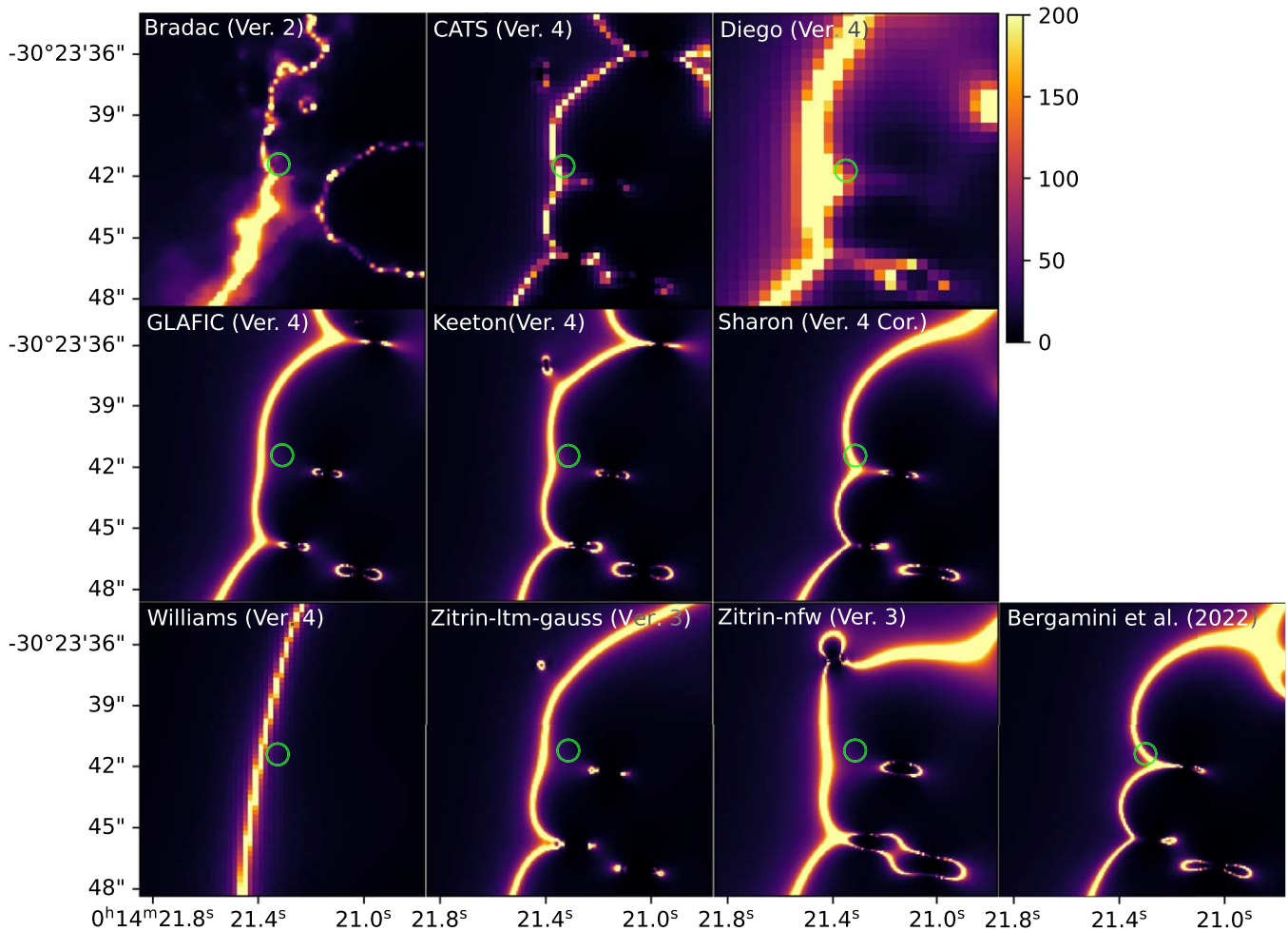
Figure 2. Magnification maps for published lens models in the vicinity of the transient. The newly discovered transient event in the JWST NIRISS imaging marked by the green circles is close to the critical curve of the galaxy cluster A2744.

location of the critical curve as shown by the green dashed line. We evaluate the magnification at the position offset by $0\rlap{.}''15$ from these models' predicted critical curve. As listed in Table 1, except Diego V4 and Zitrin-nfw V3, all the other models predict a magnification of ~100–200 at $0\rlap{.}''15$ from the critical curve, while Diego V4 and Zitrin-nfw V3 favor even greater magnifications.

Furthermore, for models with a resolution smaller than $0\rlap{.}''1\,\mathrm{pixel}^{-1}$, we compute the relative time delay between position A and its counterimage B as labeled in the inserted image in the left panel of Figure 1. We find that all the selected models predict a relative delay of less than 4 hr. This is smaller than the duration of the JWST observation. Thus, if the event were an SN in the arc, we should detect a counterimage at the B position in the JWST imaging. The nondetection of the counterimage of the transient at the other side of the critical curve allows us to exclude a multiply imaged stellar explosion.

As shown in the left panel in Figure 1, the arc is consistent with a set of multiple images (37.1, 37.2, and 37.3). According to Table A1 in Mahler et al. (2018), 37.1 and 37.2 have the same spectroscopic redshift $z = 2.6501$, while the redshift of 37.3 has not yet been confirmed.

### 3.4. Spectral Energy Distribution of the Lensed Star

We fit the spectral energy distribution (SED) of the lensed-star candidate measured from the JWST NIRISS F115W,

F150W, and F200W imaging. A stellar atmosphere model (Lejeune et al. 1998) and a host-galaxy extinction curve are simultaneously fit into the measured SED of the lensed star. As shown in Figure 3, we find the best-fit photospheric temperature of 8500 K for a Milky Way ($R(V) = 3.1$; Cardelli et al. 1989) extinction law, and the best-fit photospheric temperature of 7700 K for an SMC ($R(V) = 2.7$; Gordon et al. 2003) extinction law). Figure 3 also shows that models with 7000 K and 12,000 K temperatures are also consistent with 1σ–2σ with the measured fluxes.

3.5. Constraints on the Source Size and Magnification

The flux of the transient in the F150W and F200W imaging did not vary significantly across exposures, and hence the total time duration of the event is unconstrained. However, we can determine a lower limit on the event duration. The transient has been detected across a period of ~0.35 days (8.4 hr) from the first F150W exposure to the last F200W exposure. Thus, the duration of the microlensing peak must be >0.35 days.

At an offset of $0\rlap{.}''15$ from the galaxy-cluster critical curve near the position of the transient, we obtain $\mu \approx 200$ ($\mu_t \approx 100$, $\mu_r \approx 2$, according to the GLAFIC V4 model, where $\mu_t^{-1} = 1 - \kappa - \gamma$ and $\mu_r^{-1} = 1 - \kappa + \gamma$, and κ and γ are convergence and shear), where the Einstein radius of a microlens should be exaggerated by the cluster lens, and a microlensing
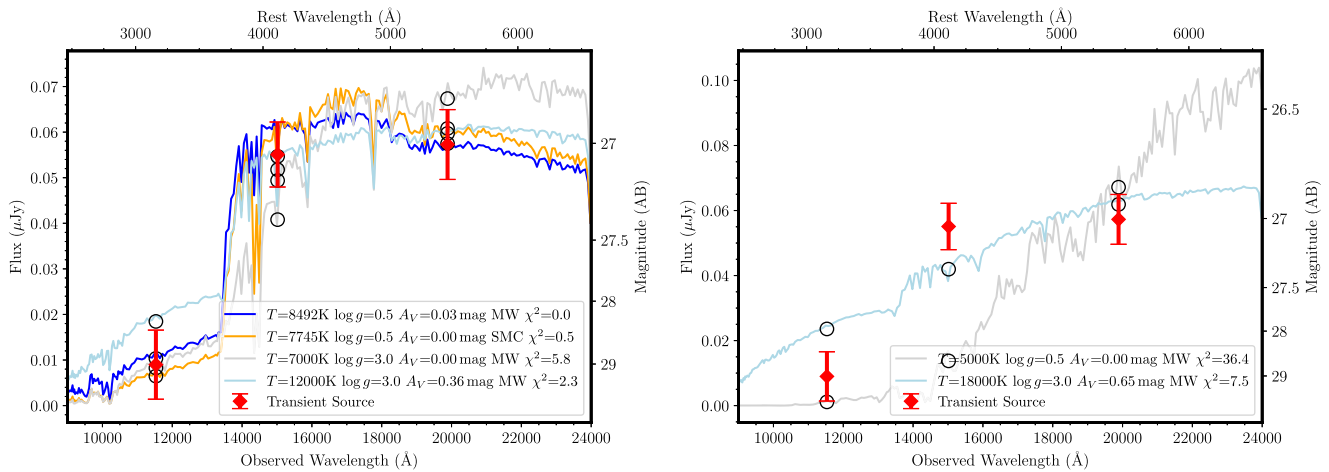
Figure 3. Stellar atmosphere models and the measured SED of the transient. The left panel shows 7000 K and 12,000 K models with an $R(V) = 3.1$ extinction law, as well as best-fitting 8500 K and 7700 K temperatures for extinction laws with $R(V) = 3.1$ and $R(V) = 2.73$, respectively. The 7000 K and 12,000 K models are consistent with the measurements within $\sim 1\sigma$–2σ. The red data points are the photometry of the transient measured from the JWST NIRISS F115W, F150W, and F200W imaging. The panel at the right shows models with 5000 K and 18,000 K where we allow the extinction to vary, and these models are in greater tension with the measurements.

peak will appear during the caustic crossing, as described in Oguri et al. (2018), Diego et al. (2018), Venumadhav et al. (2017), and Meena et al. (2022).

Oguri et al. (2018) derived a pair of equations that enable constraints on the size of the lensed source, given limits on its duration, and its maximum magnification. However, these equations only apply when the microlensing arises from a single microlens (i.e., the microcaustics are not overlapping). We measure a stellar-mass density of $11.55^{+7.61}_{-8.65}\,M_\odot\,\mathrm{pc}^{-2}$ and infer an optical depth for microlensing of $0.52^{+0.34}_{-0.39}$ at the position of the transient (as described in detail in Appendix B). Consequently, we can have a reasonable expectation that the simplified Oguri et al. (2018) analysis should yield accurate inferences. We note that Diego et al. (2018) and Venumadhav et al. (2017) provide full treatments of microlensing through simulations.

The source crossing time for the caustic-crossing event, according to Oguri et al. (2018), is given by

$$t_{\mathrm{src}} \approx 0.024 \left(\frac{R_{\mathrm{source}}}{R_\odot}\right)\left(\frac{v}{500\,\mathrm{km\,s}^{-1}}\right)^{-1}\ \mathrm{days.} \quad (1)$$

Thus, the minimum radius of the source is $14\,R_\odot \times (v/500\,\mathrm{km\,s}^{-1})$ given the minimum 0.35 day event duration and the assumption that the characteristic velocity is $500\,\mathrm{km\,s}^{-1}$. A2744 is a complex galaxy-cluster merger with a characteristic velocity of $\sim 4000\,\mathrm{km\,s}^{-1}$ (Merten et al. 2011) as inferred from measurements of the galaxies' velocities and that of the gas in the intracluster medium. The southern "clump," where we detect the transient, has a peculiar velocity of $\sim 2000\,\mathrm{km\,s}^{-1}$ as reported by Owers et al. (2011). Assuming the cluster's transverse velocity of $v = 2000\,\mathrm{km\,s}^{-1}$, the minimum radius of the source is $56\,R_\odot$. Moreover, from Equation (26) in Oguri et al. (2018), the maximum magnification during a caustic crossing for the lensing geometry of this event is given by

$$\mu_{\mathrm{max}} \approx 6.1 \times 10^4 \left(\frac{M_{\mathrm{lens}}}{M_\odot}\right)^{1/4}\left(\frac{R_{\mathrm{source}}}{R_\odot}\right)^{-1/2}, \quad (2)$$

where M_{lens} is the mass of the microlens. We note that the arc is behind the outskirt of a bright galaxy in the cluster. Assuming a microlens with $M_{\mathrm{lens}} = 1\,M_\odot$, we have the maximum magnification $\mu_{\mathrm{max}} \approx 20,000$, 6000, and 2000 for $R_{\mathrm{source}} = 10\,R_\odot$, $100\,R_\odot$, and $1,000\,R_\odot$, respectively. For $R_{\mathrm{source}} = 56\,R_\odot$, we have the maximum magnification $\mu_{\mathrm{max}} \approx 8000$. For a more massive microlens with $M_{\mathrm{lens}} \gtrsim 3\,M_\odot$, we have the maximum magnification $\mu_{\mathrm{max}} \gtrsim 10,000$.

In addition, for a solar-mass microlens and a $2000\,\mathrm{km\,s}^{-1}$ transverse velocity of the cluster lens, the time between caustic crossings (Oguri et al. 2018) will be as long as ~ 300 days.

3.6. Luminosity and Magnification of the Lensed Star

For stars of different spectral types and absolute magnitudes, we evaluate the required magnification to reach the observed apparent magnitude of 27.05 in the JWST NIRISS F150W imaging. We perform the same calculation as that in Chen et al. (2019), and our results are listed in Table 2. As we can see, based on the constraints on the minimum source size and the maximum magnification we described above, for a microlens with a few solar masses, a main-sequence star is not sufficiently luminous. A very luminous ($M_V \approx -8.5$) blue supergiant (A0 or F5) is required to explain the microlensing event that we have discovered. We note that, at lower metallicities, stars of equal temperature become comparatively more luminous.

4. Discussion

The transient we discovered in the JWST NIRISS pre-imaging can be interpreted as an extremely magnified (by a factor of $\sim 10,000$), luminous $-(9 \lesssim M_V \lesssim -7)$ blue/blue-white supergiant (Deneb-like) that was magnified by the A2744 cluster lens and a solar-mass microlens. From the best-fit SED model, as shown in Figure 3, the Balmer discontinuity at $\sim 14,000\,\text{Å}$ in the observer's frame can explain why the lensed star is only visible through the JWST NIRISS F150W and F200W filters but not detected with statistical significance in the F115W imaging.

We note that our constraints on the source size and the maximum caustic-crossing magnification are based on a solar-

Table 2
Magnification (μ) Required for Different Types of Stars

	Spec. Model	Temp	M_V	F150W	K	μ
Extreme BSG	A5	8491 K	−8.50	37.04	−1.20	9894
Extreme BSG	F0	7211 K	−8.50	37.22	−1.03	11665
MS	O5V	39810 K	−5.40	39.33	−2.01	81613
MS	O9V	35481 K	−4.00	40.80	−1.95	315414
MS	B0V	28183 K	−3.70	41.10	−1.94	416393
MS	B1V	22387 K	−3.20	41.73	−1.81	745490
MS	B3V	19054 K	−2.10	42.92	−1.72	2237247
MS	B5-7V	14125 K	−2.10	43.04	−1.61	2479165
MS	B8V	11749 K	−1.08	44.12	−1.54	6720452
MS	A5V	8491 K	2.40	47.94	−1.20	226668196
MS	F0V	7211 K	3.20	48.92	−1.03	558299929

Note. Approximate peak magnifications are for no host-galaxy extinction and for the flux density observed F150W magnitude of ∼27.05. Consequently, we favor a post-main-sequence blue/blue-white supergiant having $-9 \lesssim M_V \lesssim -7$.

mass microlens. A more massive microlens can provide higher magnification, which would allow the lensed star to be comparatively less luminous. Hence, our constraints on the luminosity and types of the lensed star will be relaxed for a massive microlens. In particular, potential populations of primordial black holes with masses of ~ 1–$100\,M_\odot$ would manifest themselves due to their action as microlenses (Diego et al. 2018). The discoveries of this kind of lensed stars in JWST and HST observations could be used to place constraints on the abundance of primordial black holes as a promising candidate for compact dark matter.

Since we observe no significant evolution in the transient's brightness, we cannot place an upper bound on the event's duration and the source size. Since most $>15\,M_\odot$ stars are observed in binary systems with a separation of $\lesssim 2000\,R_\odot$ (Sana et al. 2012, 2014), additional transients could become visible within several weeks if the source is composed of multiple stars.

A potential alternative to a luminous lensed star is a stellar-mass black hole accreting mass from an asymptotic giant branch (AGB) companion. Such systems could potentially be more common than luminous stars since the amount of time lower-mass stars spend in the AGB stage can greatly exceed the lifetimes of high-mass stars (Windhorst et al. 2018). We note that accretion disks of stellar-mass black holes may be difficult to distinguish from massive stars during microlensing events because of their similar temperatures, sizes, and luminosities. However, the continuum spectrum of an optically thick, steady-state accretion disk can be described by the integrated blackbody spectra over the disk's temperature profile, which should not exhibit a significant break in its SED at ∼4000 Å (in the rest frame) as we observed for this object. Thus, our observation does not favor a lensed stellar-mass black hole accretion disk.

It is possible, in principle, that this new transient could instead originate from the bright galaxy in the cluster. However, it is unlikely to be an SN in the galaxy cluster due to its apparent brightness and the nondetection of its rest-frame I-band flux. It is also possible, in principle, that the transient could be a multiply imaged SN where only one image has become highly magnified (or demagnified) by a microlens or

subhalo. However, extreme magnification of an SN should be extremely rare, and the large physical size of an SN photosphere means that substantial demagnification or magnification of each image by a microlens becomes improbable. Follow-up observations could constrain the duration of the microlensing event and the existence of any possible counter images.

Microlensing events with lower magnifications should be much more common than events with greater magnifications. JWST's high angular resolution, wavelength coverage in the infrared, and sensitivity should enable the collection of an extensive sample of highly magnified stars.

Appendix A
Differencing between the HST WFC3-IR and JWST NIRISS Imaging

To search for transients, we convolve and then subtract the JWST F115W and F150W imaging from coadditions of archival HST F105W and F125W images and F140W and F160W images, respectively. The JWST NIRISS imaging has a much sharper angular resolution compared to the HST WFC3-IR imaging. We therefore convolve the JWST imaging with a

transition kernel T, for which

$$\text{PSF}_{\text{JWST}} * T \approx \text{PSF}_{\text{HST}}, \tag{A1}$$

where PSF_{HST} and PSF_{JWST} are point-spread functions of the two telescopes, and $*$ denotes the convolution operation. For a source f, we have

$$(f * \text{PSF}_{\text{HST}}) \approx T * (f * \text{PSF}_{\text{JWST}}), \tag{A2}$$

where we used the commutative and associative properties of convolution. In Equation (A2), we note that $f * \text{PSF}_{\text{JWST}}$ and $f * \text{PSF}_{\text{HST}}$ are observations of f present in the JWST and HST imaging, respectively. Thus, we can utilize sources from the JWST and HST imaging to determine the kernel T.

For this paper, we determine the kernel using the Richardson–Lucy iteration algorithm (Richardson 1972; Lucy 1974). An observed image can be written as

$$d = u * P + \delta \approx u * P, \tag{A3}$$

where d, u, P, and δ are the observation, source, PSF, and noises, respectively. For an iteration number t, the estimate of u (denoted by $\hat{u}$) can be written as

$$\hat{u}^{(t+1)} = \hat{u}^{(t)} \cdot \left(\frac{d}{\hat{u}^{(t)} * P} * P' \right), \tag{A4}$$

where P' is the flipped PSF. We applied Equation (A4) on Equation (A2) to solve for T using the iteration, for which $u = T$, $d = f * \text{PSF}_{\text{HST}}$, and $P = f * \text{PSF}_{\text{JWST}}$. To minimize the accumulation of noise during the iteration, we manually selected a set of several bright (but not saturated) and isolated sources including stars and galaxies present in the imaging from both telescopes and then coadded their images for the iteration. We note that, in Equation (A2), f need not be a point source, and hence $f * \text{PSF}_{\text{JWST}}$ and $f * \text{PSF}_{\text{HST}}$ may be either images of stars or galaxies.

Appendix B
Optical Depth of Microlensing

The optical depth of microlensing (Diego et al. 2018) can be given by

$$\tau = \int_0^{D_L} \Omega_E n(D_L) dD_L, \tag{B1}$$

where Ω_E is the solid angle covered by the Einstein ring from microlenses, and $n(D_L)$ is the number density of the microlenses at an angular-diameter distance D_L. Assuming that all mass along the line of sight is concentrated in the cluster lens, Equation (B1) can be simplified as

$$\tau \approx \mu \pi \theta_E^2 n_L, \tag{B2}$$

where μ is the magnification of the macro lens from the cluster, θ_E is the Einstein radius, and n_L is the surface number density of the microlenses in the cluster lens. We note that, for point-mass microlenses, $\theta_E^2 n_L$ is proportional to the surface mass density of microlenses.

We measured the photometry in the vicinity of the transient including emissions from the wings of cluster member galaxies and from the intracluster light, and then fit it using the FAST++ software (Kriek et al. 2009; Schreiber & Dickinson 2017) to obtain the stellar mass. We obtained a surface stellar-mass density of $11.55^{+7.61}_{-8.65}$ $M_\odot$ pc^{-2}. Plugging it into Equation (B2)

(assuming solar-mass microlenses) and for $\mu \sim 10^2$, we have the microlensing optical depth of $0.52^{+0.34}_{-0.39}$ at the position of the transient.

ORCID iDs

Wenlei Chen https://orcid.org/0000-0003-1060-0723
Patrick L. Kelly https://orcid.org/0000-0003-3142-997X
Tommaso Treu https://orcid.org/0000-0002-8460-0390
Xin Wang https://orcid.org/0000-0002-9373-3865
Guido Roberts-Borsani https://orcid.org/0000-0002-4140-1367
Allison Keen https://orcid.org/0000-0002-9800-9868
Rogier A. Windhorst https://orcid.org/0000-0001-8156-6281
Rui Zhou https://orcid.org/0000-0003-0031-9241
Marusa Bradac https://orcid.org/0000-0001-5984-0395
Gabriel Brammer https://orcid.org/0000-0003-2680-005X
Victoria Strait https://orcid.org/0000-0002-6338-7295
Tom J. Broadhurst https://orcid.org/0000-0002-8785-8979
Jose M. Diego https://orcid.org/0000-0001-9065-3926
Brenda L. Frye https://orcid.org/0000-0003-1625-8009
Ashish K. Meena https://orcid.org/0000-0002-7876-4321
Adi Zitrin https://orcid.org/0000-0002-0350-4488
Massimo Pascale https://orcid.org/0000-0002-2282-8795
Marco Castellano https://orcid.org/0000-0001-9875-8263
Danilo Marchesini https://orcid.org/0000-0001-9002-3502
Takahiro Morishita https://orcid.org/0000-0002-8512-1404
Lilan Yang https://orcid.org/0000-0002-8434-880X

References

Ammons, S. M., Wong, K. C., Zabludoff, A. I., & Keeton, C. R. 2014, ApJ, 781, 2
Bergamini, P., Acebron, A., Grillo, C., et al. 2022, arXiv:2207.09416
Bradač, M., Schneider, P., Lombardi, M., & Erben, T. 2005, A&A, 437, 39
Bradač, M., Treu, T., Applegate, D., et al. 2009, ApJ, 706, 1201
Cardelli, J. A., Clayton, G. C., & Mathis, J. S. 1989, ApJ, 345, 245
Chen, W., Kelly, P. L., Diego, J. M., et al. 2019, ApJ, 881, 8
Diego, J. M., Broadhurst, T., Benitez, N., et al. 2015, MNRAS, 446, 683
Diego, J. M., Kaiser, N., Broadhurst, T., et al. 2018, ApJ, 857, 25
Diego, J. M., Protopapas, P., Sandvik, H. B., & Tegmark, M. 2005a, MNRAS, 360, 477
Diego, J. M., Sandvik, H. B., Protopapas, P., et al. 2005b, MNRAS, 362, 1247
Diego, J. M., Tegmark, M., Protopapas, P., & Sandvik, H. B. 2007, MNRAS, 375, 958
Doyon, R., Hutchings, J. B., Beaulieu, M., et al. 2012, Proc. SPIE, 8442, 84422R
Gordon, K. D., Clayton, G. C., Misselt, K. A., Landolt, A. U., & Wolff, M. J. 2003, ApJ, 594, 279
Hoag, A., Huang, K.-H., Treu, T., et al. 2016, ApJ, 831, 182
Johnson, T. L., Sharon, K., Bayliss, M. B., et al. 2014, ApJ, 797, 48
Jullo, E., Kneib, J.-P., Limousin, M., et al. 2007, NJPh, 9, 447
Kaurov, A. A., Dai, L., Venumadhav, T., Miralda-Escudé, J., & Frye, B. 2019, ApJ, 880, 58
Kawamata, R., Ishigaki, M., Shimasaku, K., et al. 2018, ApJ, 855, 4
Kawamata, R., Oguri, M., Ishigaki, M., Shimasaku, K., & Ouchi, M. 2016, ApJ, 819, 114
Keeton, C. R. 2010, GReGr, 42, 2151
Kelly, P. L., Brammer, G., Selsing, J., et al. 2016, ApJ, 831, 205
Kelly, P. L., Diego, J. M., Rodney, S., et al. 2018, NatAs, 2, 334
Kelly, P. L., Rodney, S. A., Treu, T., et al. 2015, Sci, 347, 1123
Kriek, M., van Dokkum, P. G., Labbé, I., et al. 2009, ApJ, 700, 221
Lejeune, T., Cuisinier, F., & Buser, R. 1998, A&AS, 130, 65
Liesenborgs, J., De Rijcke, S., & Dejonghe, H. 2006, MNRAS, 367, 1209
Lotz, J. M., Koekemoer, A., Coe, D., et al. 2017, ApJ, 837, 97
Lucy, L. B. 1974, AJ, 79, 745
Mahler, G., Richard, J., Clément, B., et al. 2018, MNRAS, 473, 663
McCully, C., Keeton, C. R., Wong, K. C., & Zabludoff, A. I. 2014, MNRAS, 443, 3631

Meena, A. K., Arad, O., & Zitrin, A. 2022, MNRAS, 514, 2545
Merten, J., Cacciato, M., Meneghetti, M., Mignone, C., & Bartelmann, M. 2009, A&A, 500, 681
Merten, J., Coe, D., Dupke, R., et al. 2011, MNRAS, 417, 333
Miralda-Escude, J. 1991, ApJ, 379, 94
Oguri, M. 2010, PASJ, 62, 1017
Oguri, M., Diego, J. M., Kaiser, N., Kelly, P. L., & Broadhurst, T. 2018, PhRvD, 97, 023518
Oke, J. B., & Gunn, J. E. 1983, ApJ, 266, 713
Owers, M. S., Randall, S. W., Nulsen, P. E. J., et al. 2011, ApJ, 728, 27
Richardson, W. H. 1972, JOSA, 62, 55
Roberts-Borsani, G., Morishita, T., Treu, T., et al. 2022, arXiv:2207.09416
Rodney, S. A., Balestra, I., Bradac, M., et al. 2018, NatAs, 2, 324
Rodney, S. A., Strolger, L.-G., Kelly, P. L., et al. 2016, ApJ, 820, 50
Sana, H., de Mink, S. E., de Koter, A., et al. 2012, Sci, 337, 444
Sana, H., Le Bouquin, J. B., Lacour, S., et al. 2014, ApJS, 215, 15
Schlafly, E. F., & Finkbeiner, D. P. 2011, ApJ, 737, 103
Schreiber, C., & Dickinson, H. 2017, FAST++, https://github.com/cschreib/fastpp
Sebesta, K., Williams, L. L. R., Mohammed, I., Saha, P., & Liesenborgs, J. 2016, MNRAS, 461, 2126
Treu, T., Brammer, G., Diego, J. M., et al. 2016, ApJ, 817, 60
Treu, T., Roberts-Borsani, G., Bradac, M., et al. 2022, arXiv:2206.07978
Venumadhav, T., Dai, L., & Miralda-Escudé, J. 2017, ApJ, 850, 49
Wang, X., Hoag, A. T., Huang, K.-H., et al. 2015, ApJ, 811, 29
Welch, B., Coe, D., Diego, J. M., et al. 2022, Natur, 603, 815
Windhorst, R. A., Timmes, F. X., Wyithe, J. S. B., et al. 2018, ApJS, 234, 41
Zitrin, A., Broadhurst, T., Umetsu, K., et al. 2009, MNRAS, 396, 1985
Zitrin, A., Meneghetti, M., Umetsu, K., et al. 2013, ApJL, 762, L30